Influence of the divalent and trivalent ions substitution on the structural and magnetic properties of Mg0.5−xCdxCo0.5Cr0.04TbyFe1.96−yO4 ferrites prepared by sol–gel method

Article · March 2015

CITATIONS
2

READS
132

10 authors, including:

Ghulam Mustafa
Bahauddin Zakariya University
34 PUBLICATIONS **122** CITATIONS
SEE PROFILE

Misbah ul Islam
Bahauddin Zakariya University
102 PUBLICATIONS **1,337** CITATIONS
SEE PROFILE

Abdul Waheed Anwar
University of Engineering and Technology, Lahore
35 PUBLICATIONS **166** CITATIONS
SEE PROFILE

Yasir Jamil
University of Agriculture Faisalabad
63 PUBLICATIONS **665** CITATIONS
SEE PROFILE

www.elsevier.com/locate/jmmm

Influence of the divalent and trivalent ions substitution on the structural and magnetic properties of $Mg_{0.5-x}Cd_xCo_{0.5}Cr_{0.04}Tb_yFe_{1.96-y}O_4$ ferrites prepared by sol-gel method

Ghulam Mustafa, M.U. Islam, Wenli Zhang, Abdul Waheed Anwar, Yasir Jamil, Ghulam Murtaza, Ihsan Ali, Mudassar Hussain, Akbar Ali, Mukhtar Ahmad

PII: S0304-8853(15)00335-2
DOI: http://dx.doi.org/10.1016/j.jmmm.2015.03.091
Reference: MAGMA60054

To appear in: *Journal of Magnetism and Magnetic Materials*

Received date: 30 January 2015
Revised date: 11 March 2015
Accepted date: 25 March 2015

Cite this article as: Ghulam Mustafa, M.U. Islam, Wenli Zhang, Abdul Waheed Anwar, Yasir Jamil, Ghulam Murtaza, Ihsan Ali, Mudassar Hussain, Akbar Ali and Mukhtar Ahmad, Influence of the divalent and trivalent ions substitution on the structural and magnetic properties of $Mg_{0.5-x}Cd_xCo_{0.5}Cr_{0.04}Tb_yFe_{1.96-y}O_4$ ferrites prepared by sol-gel method, *Journal of Magnetism and Magnetic Materials,* http://dx.doi.org/10.1016/j.jmmm.2015.03.091

Influence of the divalent and trivalent ions substitution on the structural and magnetic properties of $Mg_{0.5-x}Cd_xCo_{0.5}Cr_{0.04}Tb_yFe_{1.96-y}O_4$ ferrites prepared by sol-gel method.

Ghulam Mustafa*[,a], M.U. Islam[a], Wenli Zhang[b], Abdul Waheed Anwar[c] ,Yasir Jamil[d], Ghulam Murtaza[a], Ihsan Ali[a], Mudassar Hussain[a], Akbar Ali[e], Mukhtar Ahmad[f,*]

[a]Department of Physics, Bahauddin Zakariya University Multan 60800, Pakistan
[b] SKLETFID University of Electronic Science and Technology of China, Chengdu 610054 China
[c]Department of Physics, University of Engineering and Technology Lahore 54890, Pakistan
[d]Department of Physics, University of Agriculture Faisalabad 38040, Pakistan
[e]Department of Basic Sciences, Riphah International University, Islamabad-44000, Pakistan
[f]Department of Physics, COMSATS Institute of Information Technology Islamabad-44000, Pakistan

*Corresponding author: Tel: +92 333 6897526; Fax +92 61 9210068

Email addresses: ghulammustafabzu@gmail.com, ahmadmr25@yahoo.com

Abstract

A series of the divalent and trivalent co-substituted $Mg_{0.5-x}Cd_xCo_{0.5}Cr_{0.04}Tb_yFe_{1.96-y}O_4$ spinel ferrite systems (where x = 0 to 0.5 in steps of 0.1 and y = 0.00 to 0.10 in steps 0.02) are synthesized by sol-gel auto combustion method. The product materials were characterized by the thermo gravimetric analysis and differential scanning calorimetry (TGA/DSC), Fourier transform infrared spectra (FTIR), nitrogen adsorption (BET), X-ray diffraction (XRD), scanning electron microscope (SEM), atomic force microscopy (AFM) and vibrating sample magnetometer (VSM). The X-ray diffraction patterns and Fourier transform infrared spectroscopy confirm spinel nanocrystalline phase. The crystallite size is determined by Scherer's formula from 36.6 to 69.4 nm. The X-ray density is found in the range of 5.09 - 6.43 (g/cm^3). The morphological features are studied using scanning electron microscope and AFM. Saturation magnetization (Ms) and remanence (Mr) magnetization extracted from M-H loops exhibit the decreasing trends 21.4-16 emu/g and 9.1-6.3 emu/g, respectively. A significant decrease in the intrinsic parameters is observed in the prepared samples due to the weakening of the A-B interaction as iron enters into the tetrahedral A-site. The coercivity lies in the range of 300 - 869 Oe as a function of co-substitution contents. The coercivity of the sample with x=0.1, y=0.02 was found maximum i.e. 869 Oe. The obtained results suggest that the investigated materials may be potential candidates for high density recording media applications.

Keywords: Spinel ferrites; auto-combustion method; co-substitution (Cd-Tb)**;** X-ray diffraction; M-H loops.

1. Introduction

Soft magnetic materials of spinel structure are of great interest in fundamental science, especially for addressing the fundamental relationships between crystal structure chemistry and magnetic properties. These materials have unique characteristics and play an important role in various technological applications. Ferrites with higher saturation magnetization, higher electrical resistivity, and lower eddy current losses have been widely used in microwave devices [1]. The structural and magnetic properties of spinel ferrite strongly depend on the distribution of cations over the two sublattices, (A) tetrahedral and (B) octahedral sites which are occupied by different metal ions. The magnetization and the Curie temperature vary with the distribution of cations in the A and B-sites. Consequently, the magnetization in spinel ferrites changes due to the interaction between A and B-sites. The ratio of remanent magnetization to the saturation magnetization Mr/Ms varies from 0 to 1 depending upon the substitution amount of different cations into the spinel lattice. Square loops with large Mr/Ms ratio are the prime requirement in recording and memory cores [2]. Rezlescu et al, and Prasad et al [3-4] investigated the effects of rare earth ions on the ferrite structures along with their electromagnetic properties which can be changed according to requirement by substitution of different types and amounts of metal ions. Rare earth ions have unpaired 4f electrons and the strong spin-orbit coupling of angular momentum. Doping rare earth ions into spinel ferrites due to the occurrence of 4f-3d couplings which determine the magneto crystalline anisotropy in ferrites, can also improve the electrical and magnetic properties of spinel ferrites. Kolekar et al [5] reported that the cadmium doped spinel ferrites have high resistivity which is an added advantage from the point of view of developing soft ferrites. Tb^{3+} and Cd^{2+} ions have a larger ionic radius, therefore the occupancy of these ions into the spinel lattice would possibly create a lattice distortion and it is expected that all the material properties will modify to an appreciable extent. The investigated properties of these compounds depend upon the nature and size of the substitutions, as well as on the host cations owing to the cooperative behavior of these cations. Last few decades many researchers have reported the divalent and trivalent (including rare earth) ions behavior in the spinel ferrites. Cobalt base monodispersion fundamental understanding of spinel ferrites are reported by Naik et al [6]. They have prepared it by sol gel auto combustion method and observed a transition from super paramagnetic to ferromagnetic at 253K. It is noteworthy, divalent cations substituted Me-Mg-Fe (Me = Ni, Cu, Zn.) ferrites has been studied [4,7] for high-frequency applications. Similar divalent substituted elemental results are reported by Xiaogu Huang et al [8-9] and they have synthesized the [Co-Zn],[Ni-Zn] ferrite

nanofibers by electro spinning method. They observed that this is useful material for microwave absorption. Kadam et. al [10] have studied the Dy doped Ni-Co ferrite system having low coercive field suggest that these materials are suitable magnetic shielding. Amiri et.al [11] have prepared the rear earth doped Co-ferrite by the co-precipitation method. They observed that the material having highest coercivity which is suitable for hyperthermia treatment. Hashim et. al [12] have prepared In^{+3}– substituted Ni- Cu- Zn ferrites materials which are important material to develop the multilayer chip inductor (MLCIs). Furthermore some of the mixed spinel ferrite are Mg-Co-Fe-Cr [13-14],Co-Cd-Fe-Cr [15], Mg-Fe-Tb [16], Mg-Fe-Gd [17] and Mg-Fe-Dy [18] having numerous applications in electronic and microwave fields. Similarly the structural, electrical and magnetic studies of co-substitution divalent and trivalent ions in spinel ferrites like Co-Cd-Fe-Cr [19], Zn-Cu-Fe-Cr-La [20], Cu-Zn-Fe-Cr-Sm [1] and Mg-Cd-Fe-Sm have been carried out earlier [21-22]. Recently, several methods are employed to synthesize highly crystalline and uniformly sized magnetic nano-particles of ferrites. The properties of the ferrite materials are sensitive to synthesis route including chemical composition, sintering temperature, sintering time, rate of heating and cooling, as well as the amount and type of the additives ions. Different techniques exist to synthesize magnetic material, amongst them the most common are co-precipitation, hydrothermal, combustion, micro-emulsions, polymer-pyrolysis, Sol-gel [23-28] etc. The auto-combustion method has gained importance during the last few decades. This process offers many advantages compared to the conventional powder route, such as low temperature processing and better homogeneity for the synthesis of multi-component materials which leads to the formation of the nano-sized particles of ferrites. The aim of the present work is to synthesize materials with desired applications at low cost. It will be interesting to study the co-substitution of divalent and trivalent cations and its effect on the structural and magnetic behavior of soft ferrites. In the present work, we focus our investigations of $Mg_{0.5-x}Cd_xCo_{0.5}Cr_{0.04}Tb_yFe_{1.96-y}O_4$ to understand the role of co-substitution ions and their effects on the structural and magnetic behavior of these ferrites.

2. Experimental

In the present investigation, ferrite samples with chemical formula $Mg_{0.5-x}Cd_xCo_{0.5}Cr_{0.04}Tb_yFe_{1.96-y}O_4$ (with x=0 to 0.5 in steps of 0.1 and y=0.00 to 0.10 in steps 0.02) were prepared by sol-gel auto combustion method. The high purity "AR" grade materials $Mg(NO_3)_2.6H_2O$, $Cd(NO_3)_2.6H_2O$, $CoCl_2.6H_2O$, $Cr(NO_3)_3.6H_2O$, Tb_2O_3, $FeCl_3$ and citric acid $C_6H_8O_7.H_2O$ are used as starting materials for the synthesis. In order to obtain the desired compositions, the required stoichiometric amount of each

precursor material was dissolved in 100 ml of ultra-pure water. Tb_2O_3 was first dissolved in HNO_3 by heating up to 60 ^oC in a beaker and continuously stirred by a magnetic stirrer. All the prepared solutions were then added to the (chelating agent) citric acid monohydrate ($C_6H_8O_7 \cdot H_2O$) aqueous solution in 1:1.5 molar ratio to prevent agglomeration. Analytical grade liquor ammonia (30 %) was added drop wise to maintain pH value at about 7-8. The resulting solution was constantly heated at 80°C and stirred. A gel of citrate precursors was formed after 5h of continuous stirring and heating. An increase in the temperature up to 200°C led to the ignition of dry gel and a loose ferrite powder was obtained through the burning of gel in a self-propagating combustion manner. During the combustion process, exothermic decomposition of redox mixture of metal nitrates and citric acid took place along with the removal of gases such as chlorine, carbon monoxide and carbon dioxide. The obtained product was again heated at 500^oC for 2 h to remove remaining organic material present in the system and then finally ground for half an hour. The prepared dried powder was then put in alumina crucible and subsequently annealed at 850 ℃ for 8 h with a heating rate of 5 $^{\circ}$C/min in order to enhance the crystallinity of the spinel phase. Thermo gravimetric analysis and differential scanning calorimetry (TGA/DSC) were employed to analyze the thermal behaviors of the as-obtained powder. The measurements were taken on a Netzsch Sta 409 instrument, with Al_2O_3 as the inert reference material, from room temperature to 1200 ℃, at the rate of 10 ℃ min^{-1}. The Fourier transform infrared spectra (with a Model: **Jasco-310** spectrometer) were recorded in the 400–4000 cm^{-1} range. (BET) surface area and (BJH) pore size distribution were determined by N/He adsorption: Model analyzer Nova 2200e quanta chrome, USA. The X-ray diffraction (XRD) patterns were obtained at room temperature using powder samples in an Xpert Pro PANalytical diffractometer with Cu-Kα radiation (λ = 1.54056 Å) at 40 kV and 30 mA. Intensity data were collected by the step counting method (with a scanning speed 0.05°/s) in the 2θ range from 25°-65°. The surface morphology and microstructure of the samples were studied by JSM-6490 JEOL scanning electron microscope (SEM). The morphological studies were examined by using AFM (Digital instruments nanoscope-E, with Si_3N_4 100 nm cantilever, 0.58 N/m force constant measurements in contact mode. M-H loop were measured at room temperature using a vibrating sample magnetometer (VSM, Lake Shore 735) with a maximum applied magnetic field of 8 kOe.

2.1 Calculations

The structural parameters like theoretical and observed lattice constant (Å), unit cell volume, X-ray density, crystallite size 'D' lattice strain ϵ_{rms}, Ionic radii of tetrahedral and octahedral sites (r_A, r_B), bond

lengths (d_{AL} and d_{BL}), tetrahedral and octahedral hopping lengths (L_A, L_B), bond length cation-anion (Me-O) and cation-cation (Me-Me) were calculated from XRD data using the earlier reported formulae [23-26]. Moreover, Equations 1 and 2 were used to calculate the crystallite size (D) nm and root mean square lattice strain ϵ_{rms} respectively. Here k is the shape factor, λ is the X-ray wavelength and θ is the Bragg's diffraction angle and B_G is the integral width (defined as the peak area divided by peak height) of peak in radian.

$$D = \frac{k\lambda}{B_{(hkl)} \cos\theta} \qquad (1)$$

$$B_G{}^2 = 8\pi(\tan^2\theta)(\epsilon_{rms}^2) \qquad (2)$$

3. Results and discussion

3.1. Thermal analysis

Fig.1. shows the thermo gravimetric (TGA) and differential scanning calorimetric (DSC) plots of the as prepared sample that were performed up to temperature of 1200 ℃ at the heating rate of 10 ℃ min^{-1} in argon gas to observe different changes in the form of endothermic peaks and exothermic peaks which show the transformation of different phases during the heat treatment. Fig.1 reveals three ramps of mass loss around the temperature range (30 to 185 °C), (200 to 650 °C) and (650 to 1200 °C) in the TGA curve. The first weight loss at around 97 °C with an endothermic peak in DSC is attributed to loss of free water or moisture. The second one extending from 200 to 270 °C could be ascribed to the decomposition of citric acid, removal of trapped water or water of crystallization and followed by sustained mass loss from 300-520 °C due to combustion of residual organic components. The TGA curve pattern is linear from 650 to 1200 °C and after it no more weight loss took place which reflects the formation of nano-crystalline spinel ferrite. The overall weight loss is 43.76% of the product at 1200 °C**.** Together with the results from the FT-IR, we can conclude that the organic compounds were eliminated above 500 °C and bonds between metal and oxygen were formed.

3.2. IR spectra

Fig. 2 shows the FTIR spectra for the annealed samples (x= 0.02, 0.06, 0.10) recorded in the range of 400-4000 cm^{-1} and the common features of investigated ferrite spectra exhibit absorption peaks below 600 cm^{-1} that represent metal oxygen (M-O) vibration mode [33]. In FTIR spectra of the investigated samples, the characteristics of the tetrahedral sites (A-O_4) have high frequency peaks with metal–oxygen

(M-O) stretching lies at around 532.2cm^{-1}, 534.2cm^{-1}, and 528.4cm^{-1}. The low frequency peaks are observed at about 420.7cm^{-1}, 424cm^{-1}, and 453.8cm^{-1} that correspond to the characteristics of the octahedral sites (B-O_6), which reflects the local lattice effect in the octahedral sub-lattice. The presence of the absorption peaks observed at these frequencies confirm the single phase formation of the investigated ferrites and that there is no peak that may correspond to the impurity phase.

3.3 Sorbent Characterization

The plots for specific surface area pore size distribution, total pore area and total pore volume by the analysis of Brunauer Emmett and Teller (BET) or Barrett Joyner Halenda (BJH) nitrogen adsorption and desorption isotherms on mesoporous or microporous materials are shown in the Fig.3 (a-d). The surface area of the precursor is found to be 61.7, 114.3 and 116.1m^2/g. Similarly, from the BHJ method, it is reflected from the plot that with adsorption the selected samples have surface area 105.1, 11.6 and 13.2 m^2/g. The average diameter, d_{BET} is calculated by BET method as [34]:

$$d_{BET} = 6/A_s\, d_\rho \qquad (3)$$

Where A_s is the specific surface area (m^2/g) an d_ρ is the theoretical bulk density of the material (2.8 g/cm^3). The observed pore diameter values are equal to 124.8, 68.3 and 122.6 Å respectively. The observed particles size of mechanical activated ferrite is determined by BET technique while the equivalent spherical diameter is 34.7, 18.74 and 18.46 nm.

3.4. XRD measurements and SEM images

Fig.4 shows X-ray diffraction patterns of $Mg_{0.5-x}Cd_xCo_{0.5}Cr_{0.04}Tb_yFe_{1.96-y}O_4$ spinel ferrite system (where x = 0 to 0.5 in steps of 0.1 and y = 0.00 to 0.10 in steps 0.02). The crystalline phases of all the samples were developed by annealing at 850 $^{\circ}$C for 8 h. The diffraction peaks at (220), (310), (311), (333), (400), (440) and (511) planes confirm the formation of cubic spinel ferrite. All the observed peaks were indexed by Jade 5 software. It was observed that the first three samples (Cd^{2+}, Tb^{3+}) = (x, y) = 0.0, (0.1, 0.02) and (0.2, 0.04) revealed fcc single phase, however remaining three samples (x, y) > (0.2, 0.04) reflected secondary phase at 33^o (2θ value) as shown in the X-ray diffraction patterns. For (x, y) > (0.2, 0.04), this second phase $TbFeO_3$ with (310) reflection plane is named as orthoferrite phase. This secondary phase on grain boundaries appears due to high reactivity of Fe^{+3} ions with co-substituted contents [35]. The value of the lattice parameter for the present samples lies in the range of 8.369 - 8.457Å (Table 1). It is observed that the lattice constant increases with the increase of co-substitution (x,

y) contents up to (0.2, 0.04) and (0.4, 0.08). This increase in lattice constant is due to the partial incorporation of the co-substitution (Cd^{2+}, Tb^{3+}) contents into the spinel lattice as the ionic radii of Cd^{2+} (0.84 Å) and Tb^{3+} (0.93 Å) ions are the larger than the ionic radii of Fe^{3+} (0.67Å) [16,36-37].This can be explained on the basis of the relative ionic radii and attractive forces between oxygen and the cations. So the competition between the ionic radii and attractive forces is responsible for the observed variation of the lattice parameters. At (x, y) = (0.1, 0.02), (0.3, 0.06) and (0.5, 0.10), the lattice constant and cell volume (Table 1) of the unit cell decrease which may be attributed to the segregation of the co-substitution ions at the grain boundaries and due to the difference of the ionic radii, atomic mass of the elements and creation of vacancies that cause lattice distortion. Another, possible reason of the spinel lattice compression may be the differences in the thermal expansion coefficients, intergranular secondary phase thereby giving an indication of existence of a solubility limit for Tb^{3+} ions [38]. The crystallite size is calculated using Scherrer's formula and the results is found in the range 36.6-69.4 nm (Table1) and there is similar result reported earlier 40–75 nm for the spinel ferrites synthesized by sol–gel method [33]. It has been reported that the crystallite size below 50 nm is useful in obtaining the suitable value of signal-to-noise ratio in the high density recording media [39]. In the present study the crystallite sizes were found below 50 nm for all the materials except at (x, y) = (0.2, 0.04), (0.3, 0.06) and (0.5, 0.10), so the materials with size below 50 nm can be useful in obtaining suitable signal-to-noise ratio value in high density recording media. The increase in X-ray density (Table 1) by (x, y) co-substituted samples is due to the larger atomic mass of the samples i.e.; Cd^{2+}; (112.41 $gmol^{-1}$), Co^{2+}; (58.93 $gmol^{-1}$), Cr^{3+}; (51.99 $gmol^{-1}$), and Tb^{3+}; (158.92 $gmol^{-1}$) respectively which are larger as compared to those for Mg^{2+}; (24.31 $gmol^{-1}$) and Fe^{3+}; (55.84 $gmol^{-1}$). The X-ray density being dependent upon molecular weight and lattice constant of samples, exhibits an increasing trend 586.07 - 602.77 g/cm^3. On the other hand, there is minor deviation from the lattice strain (Table 1) which decreases from 2.7×10^{-3} to 1.1×10^{-3}.

The XRD data was further used to calculate theoretically lattice constant by a careful selection of cations in the octahedral and tetrahedral sites by the relation [40]:

$$a_{th} = \frac{8}{3\sqrt{3}}(r_A + r_O) + \sqrt{3}(r_B + r_O) \qquad (4)$$

Where r_0 is the oxygen ions radius of the (1.32 Å). The theoretical values of the lattice constant (a_{th}) as a function of concentration (x, y) are listed in Table 2. It is seen that there is reasonable agreement between experimental and theoretical values of lattice constant suggesting that the estimated cation

distribution is in agreement with real distribution in that range. The experimental error (the difference between theoretical and experimental lattice constant) increases with increasing co-substitution (x, y). The increase in the difference with co-substituted indicates the possibility of the effects like ‘‘covaliancy’’, which is not considered in the theoretical model. In cation distribution, there are two extreme types, normal spinel $\left(\mathrm{Me}^{2+}\right)_{\mathrm{A}}[\mathrm{Fe_2}^{3+}]_{\mathrm{B}}\,\mathrm{O}_4$ and inverse-spinel $\left(\mathrm{Me_x}^{2+}\,\mathrm{Fe}_{1-\mathrm{x}}{}^{3+}\right)_{\mathrm{A}}[\mathrm{Me}_{1-\mathrm{x}}{}^{2+}\,\mathrm{Fe}_{1+\mathrm{x}}{}^{3+}]_{\mathrm{B}}\mathrm{O}_4$ where the parentheses and brackets refer to cations occupying the tetrahedral A-sites and the octahedral B- sites, respectively. The cation distribution strictly followed rules to calculate lattice constant which are as follows: (i) A site has a sum of cationic distribution equal to one (1) and that for B site is considered as equal to two (2), (ii) It is assumed that Cd^{2+}, Co^{2+}, and Fe^{3+} ions occupy the A-sites and Mg^{2+}, Co^{2+}, Cr^{3+} and Tb^{3+} ions have more preference to B site and B site is assumed to have Fe^{2+} ions. Using these conditions, the proposed distribution of cations provides one to one correspondence of theoretical and experimental values [7]. The tetrahedral and octahedral distances, ionic radius, bond lengths and hopping lengths ware calculated by the following relations [19, 41-42] and the obtained values are listed in Table2.

$$\mathrm{r_A} = \sum_{i=1}^{n} x_i\,(Me_i - O)_{tetra} \qquad (5)$$

$$\mathrm{r_B} = \frac{1}{2}\sum_{i=1}^{n} y_i\,(Me_i - O)_{octa} \qquad (6)$$

$$\mathrm{d_{AL}} = \mathrm{a}\sqrt{3}\,(\mathrm{u} - 0.25) \qquad (7)$$

$$\mathrm{d_{BL}} = \mathrm{a}\sqrt{3\mathrm{u}^2 - \frac{11}{4}\mathrm{u} + \frac{43}{64}} \qquad (8)$$

$$\mathrm{L_A} = \mathrm{a}\frac{\sqrt{3}}{4} \qquad (9)$$

$$\mathrm{L_B} = \mathrm{a}\frac{\sqrt{2}}{4} \qquad (10)$$

From (Table 2) values revealed that the mean tetrahedral and octahedral site ionic radius increases with increasing co-substitution (x, y). This is due to the replacement of larger ionic radii (Fe^{3+}) with smaller ionic radii (Cr^{3+}) and their distribution amongst the A- and B-sites. Moreover, the inter ionic distances $(\mathrm{d_{AL}}, \mathrm{d_{BL}})$ of the tetrahedral and octahedral interstitial sites increase with increasing co-substitution (x, y) contents and the obtained results are consistent with the reported data [43]. Table 2 shows the relation between the hopping lengths in tetrahedral and octahedral sites as a function of co-substitution (x,y) content. The distance between the magnetic ions increases as the (x,y) content increase. This may be explained on the basis of difference in ionic radii of substituent ions.

In addition, the bond lengths between the cations (b, c, d, e and f) (Me–Me) and between the cation and anion (p, q, r and s) (Me–O) were calculated using the experimental values of lattice constant by the relations [43]:

$(Me-O)$ Å	$(Me-Me)$ Å
p = a (1/2 - μ)	b = (a/4) $2^{½}$
q = a (μ - 1/8) $3^{½}$	c = (a/8)$11^{½}$
r = a (μ - 1/8) $11^{½}$	d = (a / 4) $3^{½}$
s = a/3 $(μ + 1/2)3^{½}$	e = (3a/8) 3 ½
f = (a/4) 6 ½	

where the oxygen positional parameter (μ) for each composition is 0.381[36]. The observed results show that the decrease in Me–O and the results of Me–Me distances illustrate the enhancement of strength of magnetic interactions. But the replacement of magnetic Fe^{3+} by non-magnetic $Mg^{2+}$and Tb^{3+} reduces the strength of magnetic interactions in the system (Table 3).

Fig.5 (a and b) respectively shows the morphologies of the selected samples examined by SEM. The particle size was estimated from SEM images by using the line intercept method. The investigated sample Tb_2O_3 has a bi-phase microstructure with bigger matrix and smaller particle size. The average particle size was found to be in the range of a few microns (μm) for the representative samples of these ferrites. The similar results were reported earlier by Roy et al [44]. The shape of the materials is very important for various applications in different field and it can be used in catalysis, information storage, surface enhanced Raman scattering, imaging sensing and memory core. The particles have well-defined spherical, shape and agglomerated to some extent because of magnetic dipole interactions between ferrite particles. In view of the fact that the crystallite sizes calculated by the Scherrer formula are not considered being very accurate, therefore we have determined the particle size from the SEM micrographs.

3.5 Atomic Force Microscopy

Fig.6 shows the AFM images of the samples which give the complimentary information about the surface microstructure, particles size distribution and shape of samples synthesized by sol-gel method. It is observed that the composition of the sample has uniform morphology and is of spherical shape with

the average size less than 55 nm. The appearance of nanometer-sized grain observed by AFM was also consistent with the results of SEM analysis.

3.6 Magnetic measurements

Fig. 7 shows the M versus H curves of $Mg_{0.5-x}Cd_xCo_{0.5}Cr_{0.04}Tb_yFe_{1.96-y}O_4$ spinel ferrites powder annealed at 850 ^oC. The saturation magnetization was measured for each sample at room temperature in the applied magnetic field 8 KOe. The values of both saturation magnetization and remanance are found in the range of 21.4-16.3 emu/g and 9.1-5.9 emu/g, respectively with (x, y) co-substitution content and are given in Table 4. The observed decreasing trend in saturation magnetization can be explained on the basis of cation distribution and the exchange interactions between A and B-sites respectively. Similar results are reported for rare earth substituted spinel ferrites by J. Jiang et al [45]. It shows that all Cd^{2+} ions occupy A-site, Tb^{3+} ions preferably enter B-site octahedral when a small fraction of Tb^{3+} ions replace Fe^{3+} ions at B-sites. As the number of Fe^{3+} at B-sites decreases by the replacement of Tb^{3+} ions, the magnetization of B-sublattice decreases, resulting in the decrease in magnetization for the Tb^{3+} ions substituted ferrites. The magnetic moment n_B was also calculated from magnetization data recorded at room temperature using the following relation [46];

$$n_B(\mu_B) = \frac{\text{Molecular Weight} \times M_s}{5585} \qquad (11)$$

The calculated magnetic moment values are listed in Table 4. The results show that the magnetic moments of the rare earth ions usually originate from the localized 4f electrons at room temperature with their magnetic dipolar orientation is disordered. Therefore it can be assumed that Tb^{3+} ions are non-magnetic ions having no contribution to the magnetization of substituted ferrite at room temperature.

Table 4 shows that the value of the magnetic moments is decreasing linearly with increasing (x,y) co-substitution in these samples which is quite consistent with the behavior of saturation magnetization. The gradually decrease of magnetic moment n_B is found in the entire sample. According to Ladgaonkar at el. [47] polycrystalline magnetic material consists of three types of domain states. The remanance ratio (Mr/Ms) for all the samples is observed in the range of 0.35 to 0.47 (well below of typical value ~1) [48]. Fig.8 shows the variation of saturation magnetization and coercive field with different (x, y) co-substituted contents. It is observed that coercive force is in the range of 300-869 Oe (Table 4) and increasing (x, y) content and the magnitude of coercive force also decreases. Another reason for decrease of coercive force is the microstructure property in which surplus Tb^{3+} ions locating at the grain boundaries form secondary phase. This secondary phase at the grain boundaries hinders the motion of

the magnetic domain walls and induces some distortion within the grains. [35,49]. The saturation magnetization M_s and coercivity H_c are related to each other by the Brown's relation [50]:

$$H_C = \mp \frac{2K_1}{\mu_o M_s} \quad (\mathbf{12})$$

Where K_1 is the anisotropy constant, μ_o is vacuum permeability and Ms represents the saturation magnetization. It is evident from the equation that both coercivity (H_c) and saturation magnetization (M_s) are inversely proportional to each other. Anisotropy constant (k_1) was calculated by using the relation ($K_1=\mu_o H_c M_s/2$). In this case, it was assumed that the magnetic particles have the characteristics of single domains. Moreover they are isolated in terms of exchange interacting spin [51].The determined values of anisotropy constant (k_1) is listed in Table 4 for all the samples.

Conclusions

XRD patterns revealed that the first three samples have fcc single phase where as rest of other samples reflect biphasic trend. The lattice constant was found in the range of (8.369 -8.457Å). The decrease in lattice constant at (x,y) ≥ (0.3,0.06) indicated the solubility limit of Tb^{3+} in the spinel lattice. The BET method shows mechanical activated ferrite precursor powders having diameter of 34.7, 18.74 and 18.46 nm. The average crystallite sizes of all the samples are calculated using Scherrer's formula and are found in the range of 36.6-69.4 nm. The AFM and SEM are also employed to confirm the morphology of the synthesized materials. The saturation magnetization and magnetic moment were found in decreasing trend with increasing (Cd^{2+}, Tb^{3+}) co-substituted content in spinl ferrite. Magnetic properties revealed that there exists a small anisotropy. Squareness ratio indicates that the substitution of Tb^{3+} resulted rise in the cubic magnetocrystalline anisotropy and subsequently grain–grain interaction is enhanced. The coercivity and remanent also decreases with increasing (x, y) co-substituted content while, the maximum coercivity was observed at (x,y) = (0.1, 0.02) 869 Oe which is ≥ 600Oe. The magnetic properties of (x,y) co-substituted Mg–Co-Cr-Tb ferrites are changed in comparison with pure ferrites. The observed values of these parameters show that the materials can be used in number of applications like high density recording media.

Acknowledgements

One of the authors (Ghulam Mustafa) is thankful to Higher Education Commission (HEC) of Pakistan for the financial assistance under HEC International Research Support Initiative Program (IRSIP).

References

[1] Li Liangchao , Qiu Haizhen ,Wang Yuping, Jiang Jing, Xu Feng, J.Rare Earths 26(4) (2008) 558.

[2] S.A. Masti, A.k.Sharam, P.N.Vasambekar, A.S.Vaingankar, J. Magn. Magn. Mater. 305 (2006) 436-439.

[3] N. Rezlescu, E. Rezlescu, Solid State Commun. 88 (1993) 139 –141.

[4] M. Siva Ram Prasada, B.B.V.S.V. Prasad, B. Rajesh, K.H. Rao, K.V. Ramesh, J. Magn. Magn. Mater. 323 (2011) 2115-2121.

[5] C.B.Kolekar. P.N.Kamble,A.S Vaingankar, J. Magn. Magn. Mater. 138 (1994) 211-215.

[6] S. R. Naik, A. V. Salker, S. M. Yusuf, S. S. Meena, J. Alloy. Comp. 566 (2013) 54-61.

[7] A. Pradeep, G. Chandrasekaran, Mater. Lett. 60 (2006) 371-374.

[8] Xiaogu. Huang, Jing Zhang, Min Lai, Tianyi Sang, J. Alloy. Comp. 627 (2015) 367-373.

[9] Xiaogu Huang, Jing Zhang, Shaorang Xiao, Guosheng Chen, J. Am. Cerm. Soc. 97 (2014)1363-1366

[10] A. A. Kadam, S. S. Shinde, S. P. Yadav, P. S. Patil, K. Y. Rajpure, J. Magn. Magn. Mate. 329 (2013) 59-64.

[11] S. Amiri, H. Shokrollahi, J. Magn. Magn. Mate.345 (2013)18-23.

[12] Mohd Hashim, Alimuddin, Sagar E. Shirsath, Shalendra Kumar, Ravi Kumar, Aashis S. Roy, Jyoti Shah, R. K. Kotnala, J. Alloy. Comp, 549 (2013) 348-357.

[13] S.J. Shukla, K.M. Jadhav, G.K. Bichile, J. Magn. Magn. Mater. 195 (1999) 692-698.

[14] Muhammad Javed Iqbala, Zahoor Ahmad, Turgut Meydan, Yevgen Melikhov,J. Magn. Magn. Mater. 324 (2012) 3986-3990.

[15] P.N. Vasambekar, C.B. Kolekar, A.S. Vaingankar, Mater. Chem. Phys. 60 (1999) 282-285.

[16] M. Azhar Khan,M.U. Islam, M. Ishaque, Ceram.Int. 37 (2011) 2519-2526.

[17] Jag dish Chand, M. Singh, J. Alloy. Comp. 486 (2009) 376-379.

[18] K.K. Bamzai, Gurbinder Kour, B. Kaur, S.D. Kulkarni, J. Magn. Magn. Mater.327 (2013) 159-166.

[19] A.R. Shitre, V.B. Kawade, G.K. Bichile, K.M. Jadha, Mater. Lett.56 (2002) 188-193.

[20] Liangchao Li, HuiLiu, Yuping Wang, Jing Jiang, FengXu, J.Colloid Interface Sci.321 (2008) 265-271.

[21] A.B.Gadkari,T,J.Shine,P.N.Vasambekar, Mater. Charact. 60 (2009) 1328-1333.

[22] Ashok B. Gadkari, Tukaram J. Shinde, Pramod N. Vasambekar, J. Magn. Magn. Mater 322 (2010) 3823-3827.

[23] D.R. Cornejo, A. Medina. Boudri, J. Matutes Aquino, Physica B 320 (2002) 270-273.

[24] Xie Yi, Qian Yitaia, Li Jinga, Zuyaoa, Yang Li, Mater. Sci. Eng. B 34 (1995) 1-3.

[25] Kashinath C.Patil, S.T. Aruna,Tanu Mimani, Curr.Opin.Solid State Mater.Sci. 6 (2002) 507-512.

[26] V. Pillai, D.O. Shah, J. Magn. Magn. Mater, 163 (1996) 243-248.

[27] Xian.Ming Liu,Shao.Yun Fu,Hong.Mei Xiao,Chuan.Jun huang Pysicsa B, Condens. Matter, 370 (2005) 14-21.

[28] Woo Chul Kim, Seung Wha Lee, Sam Jin Kim,Sung Hyun Yoon,Chul Sung kim, J. Magn. Magn. Mater, 215-216 (2000) 217-220.

[29] B.D. Cullity, Second Edition Addison Wesley Publishing, Co; (1978) pp 42-46, 89, 92-102

[30] R.E. Smallman, K.H.G.Ashbee, Paragon press London (1969) p. 77-78.

[31] Ghulam Mustafa,M.U.Islam,Wenli Zhang,Yasir Jamil, Abdul Waheed Anwar ,Mudassar, Hussain, Mukhtar Ahmad, J. Alloy Comp. 618 (2015) 428–436.

[32] Ghulam Mustafa,M.U.Islam,Wenli Zhang,Yasir Jamil,M.Asif Iqbal,Mudassar Hussain,Mukhtar Ahmad, J. Magn. Magn. Mater. 378 (2015) 409-416.

[33] A. M. El-Sayed, Ceram. Int. 28 (2002) 651-655.

[34] R.A. Candeia, B. Bernardi, E. Longo, G. Santos, A.G. Souza, Mater. Lett. 58 (2004) 569 – 572.

[35] R.V. Upadhayay, R.V. Mehta, K. Prakash, D. Srinivas, R.R. Pant, J. Magn. Magn.Mater. 201 (1999) 129.

[36] K.J. Standly, Oxide Magnetic Material, Clarendon Press, Oxford, 1972.

[37] Binu P. Jacob, Smitha Thankachan, Sheena Xavier, E.M. Mohammed, J. Alloy. Comp. 578 (2013) 314–319.

[38] J.F. Wang, C.B. Ponton, R. Grossinger, J.R. Harris, J. Alloys Compd. 369 (2004) 170.

[39] Muhammad Jhaved Iqbal,Mah Rukh Siddiquah, J. Magn. Magn. Mater. 320 (2008) 845-850.

[40] Muhamamd Naeem Ashiqa, Muhammad Fahad Ehsan, Muhammad Javed Iqbal, Iftikhar Hussain Gul, J. Alloy.Comp. 509 (2011) 5119-5126.

[41] C. Venkataraju, G. Sathishkumar, K. Sivakumar, J.Magn. Magn. Mate 322 (2010) 230–233.

[42] Lu Xiao, Tao Zhou, Jia Meng, Particuology,7 (2009), 491-495.

[43] R. L. Dhiman, S. P. Taneja, and V. R. Reddy, Advances in condensed Matter physics (2008) P-7

[44] K.B. Modi, J.D. Gajera, M.C. Chhantbar, K.G. Saija, G.J. Baldha, H.H. Joshi, Mate Lette. 57

(2003) 4049- 4053.

[45] P.K.Roy,Bibhuti B.nayak,j.Bera, J. Magn. Magn. Mater. 320 (2008) 1128-1132.

[46] Jing Jiang, Chaochao Chen and Lunhong Ai, Inter. J. Modern Physics B, 24 (2010) 5409 –5416.

[47] P.P. Hankare, S.D. Jadhav, U.B. Sankpa, K.J. Waghmare, B.K. Chougule, J. Alloy.Compd. 475 (2009) 926–929.

[48] B.P.Ladgaonkar, P.N.Vasambekar, A.S.Vaingankar, J. Magn. Magn. Mate. 210 (2000) 289-294.

[49] Daliya S.Mathew,Ruey Shin juang ,Chemical Engineering Journal 129 (2007) 51-65.

[50] S.E.Shirsath,B.G.Toksha,K.M.Jadhav,Mater.Chem.Phys. 117 (2009) 163-168.

[51] J.M.D. Coey, J.Magn.Magn.Maer. 196-197 (1999) 1-7.

[52] Xiaofei Cao, Kangning Sun, Chang Sun, Liang Leng, J. Magn. Magn. Mater. 321 (2009) 2896.

List of Figures

Fig.1.TGA and DSC curves of the $Mg_{0.5-x}Cd_xCo_{0.5}Cr_{0.04}Tb_yFe_{1.96-y}O_4$ ferrite powder (where x = 0.5 and y = 0.10) from room temperature to 1200 ^oC.

Fig.2. FTIR spectra of the co-substituted (Cd^{2+} Tb^{3+}) content Mg-Co-Cr-Fe-O ferrites.

Fig.3. Shows the BET surface area and BJH pore size distribution of the powders which are heat treated 300 ^oC**.**

Fig.4. X-ray diffraction of $Mg_{0.5-x}Cd_xCo_{0.5}Cr_{0.04}Tb_yFe_{1.96-y}O_4$ ferrite powders annealed at 850 ^oC for 8h.

Fig.5. SEM micrographs of the $Mg_{0.5-x}Cd_xCo_{0.5}Cr_{0.04}Tb_yFe_{1.96-y}O_4$ ferrites at co-substitution (x,y) = (0.2,0.04) and (0.3,0.06) content.

Fig.6. AFM images of $Mg_{0.4}Cd_{0.1}Co_{0.5}Cr_{0.04}Tb_{0.02}Fe_{1.94}O_4$ spinel ferrite.

Fig.7. M-H loops for $Mg_{0.5-x}Cd_xCo_{0.5}Cr_{0.04}Tb_yFe_{1.96-y}O_4$ ferrite powders annealed at 850 ^oC.

Fig.8. Variation of saturation magnetization and coercive field with different co-substituted (Cd^{2+} Tb^{3+}) content for Mg–Co-Cr-Fe ferrites system.

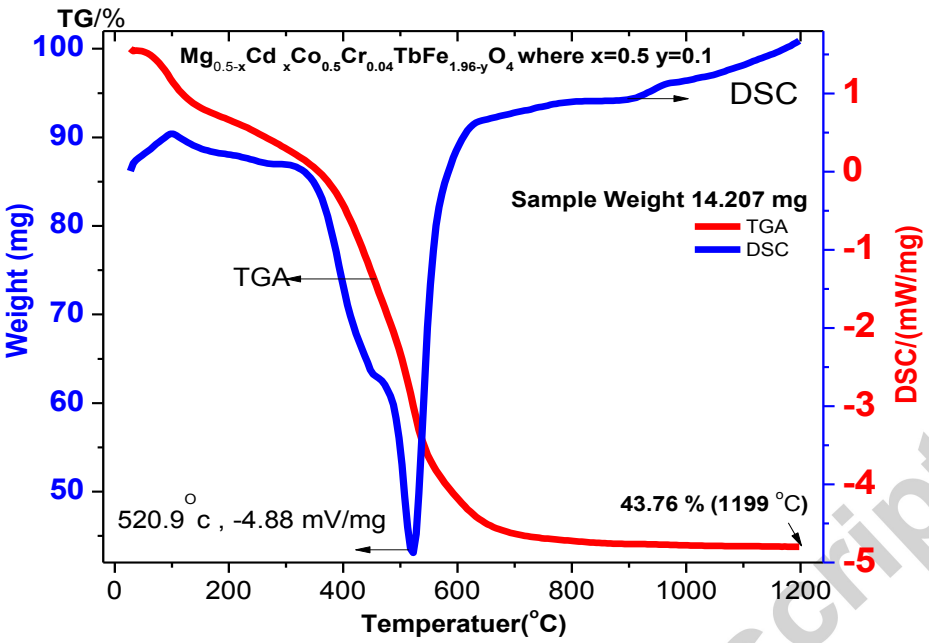

Fig.1. TGA and DSC curves of the $Mg_{0.5-x}Cd_xCo_{0.5}Cr_{0.04}Tb_yFe_{1.96-y}O_4$ ferrite powder where x=0.5 and y=0.10 from room temperature to 1200 °C.

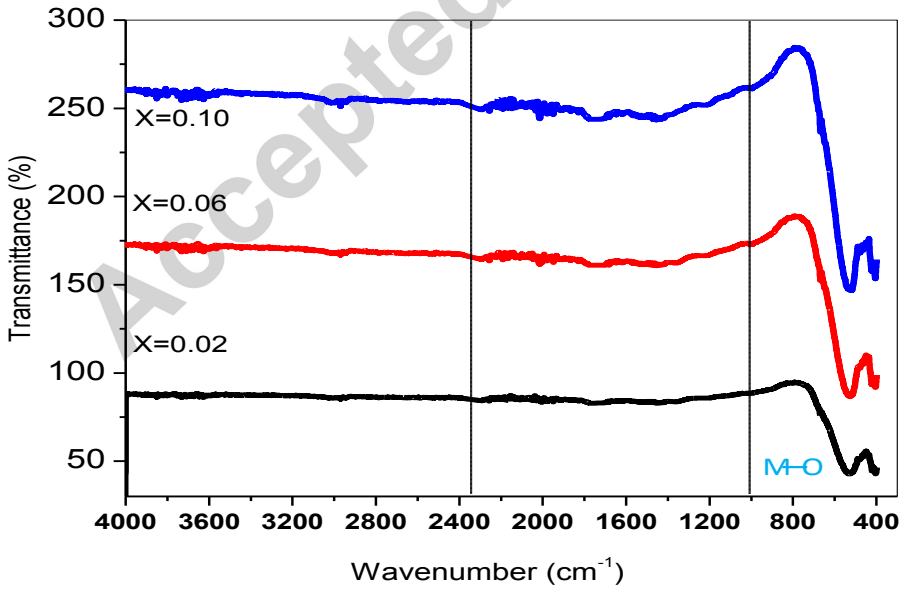

Fig. 2. FTIR spectra of the (Cd-Tb) co-substitution Mg-Co-Cr-Fe-O ferrites.

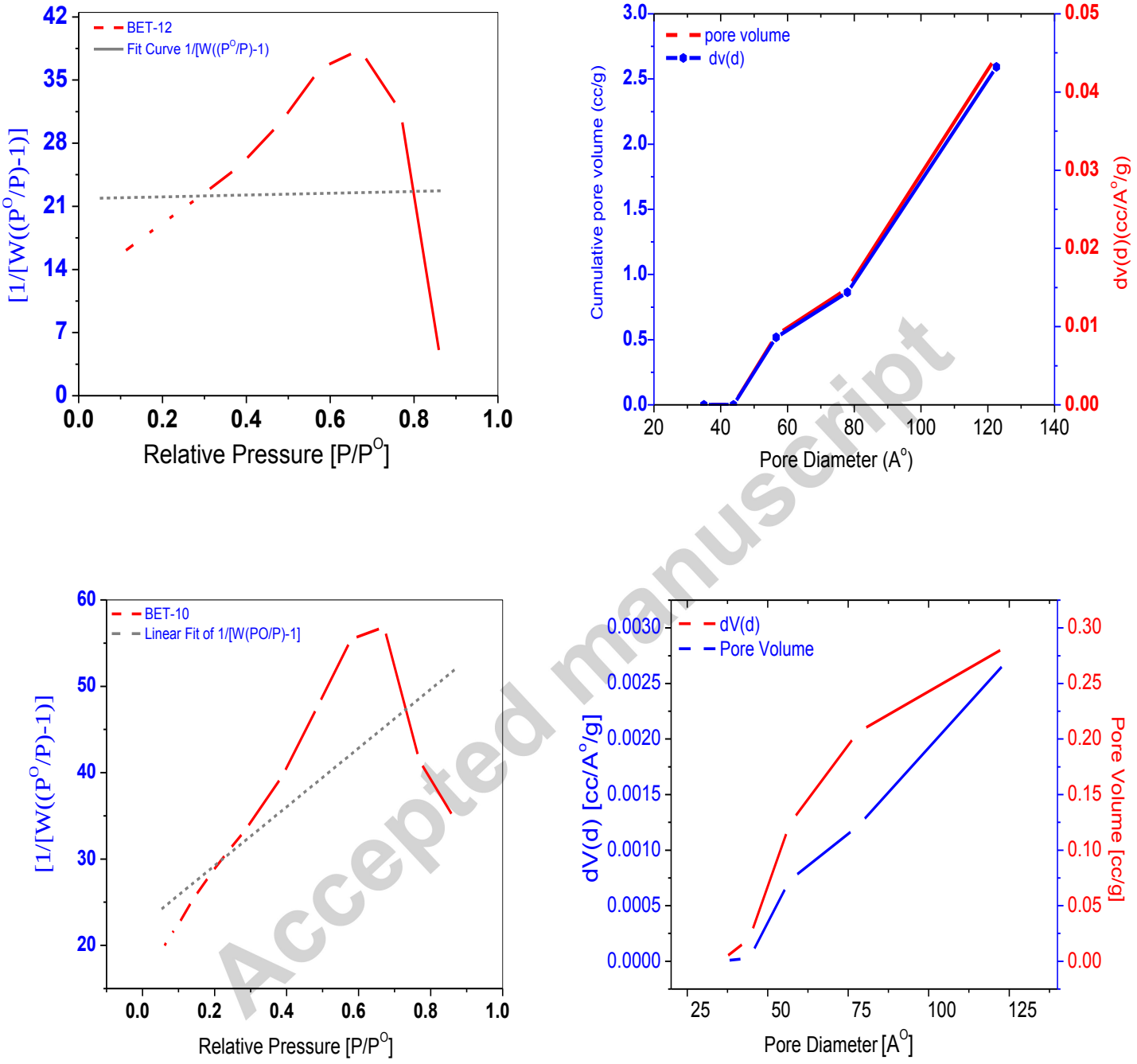

Fig.3. (a-d) shows the BET surface area and BJH pore size distribution of the powders which are heat treated at 300^{o}C**.**

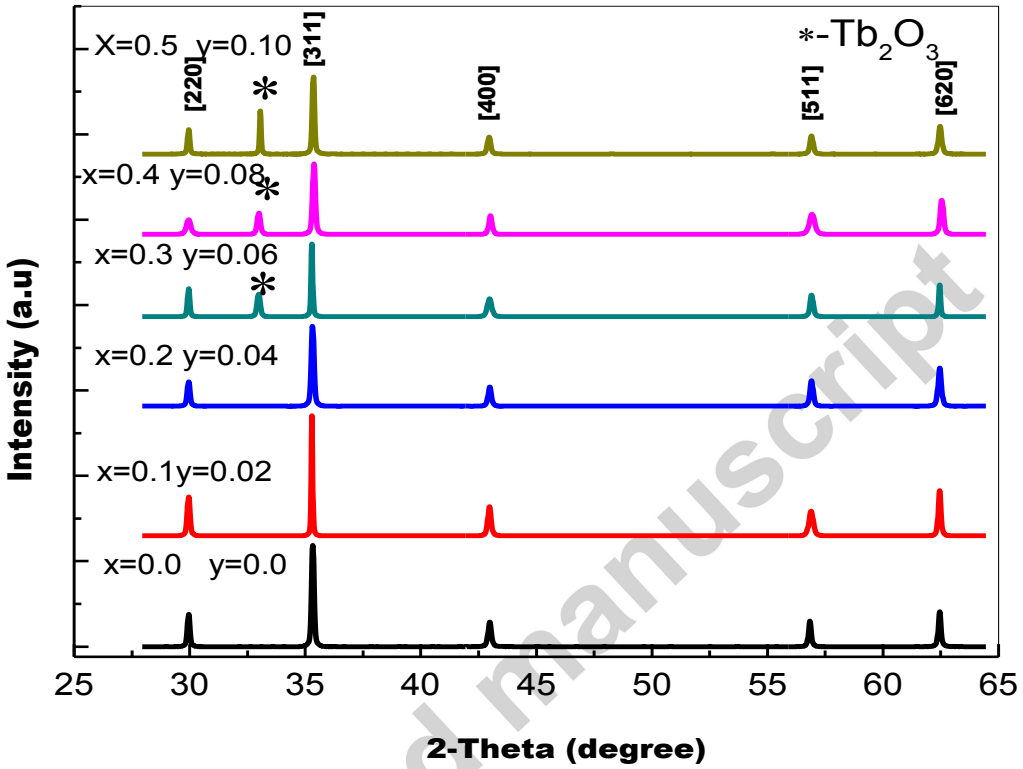

Fig.4. X-ray diffraction of $Mg_{0.5-x}Cd_xCo_{0.5}Cr_{0.04}Tb_yFe_{1.96-y}O_4$ ferrite powders annealed at 850 ^oC for 8h.

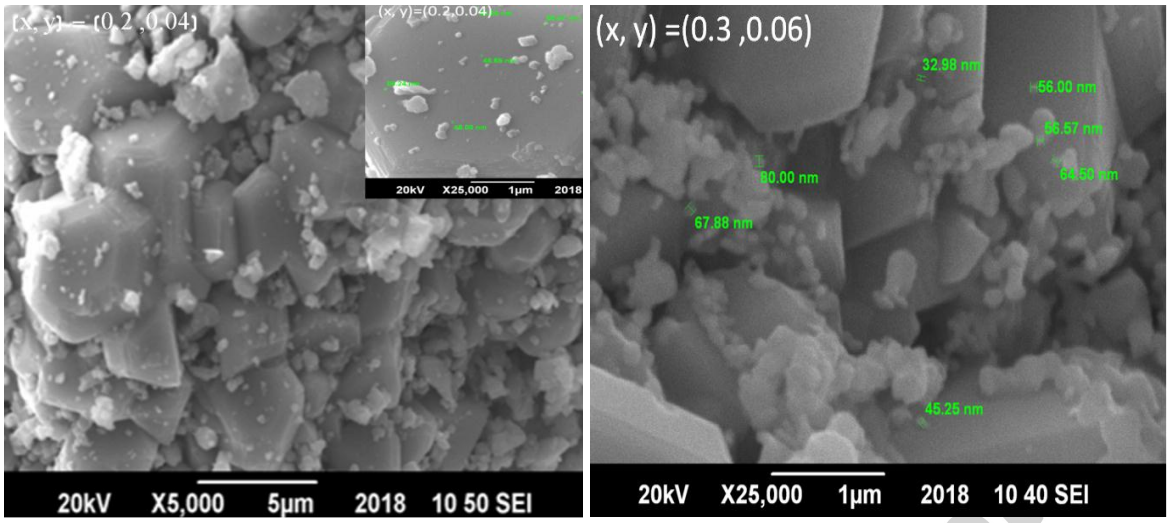

Fig.5. SEM images of the $Mg_{0.5-x}Cd_xCo_{0.5}Cr_{0.04}Tb_yFe_{1.96-y}O_4$ ferrites at (x,y) = (0.2,0.04) and (0.3,0.06) content.

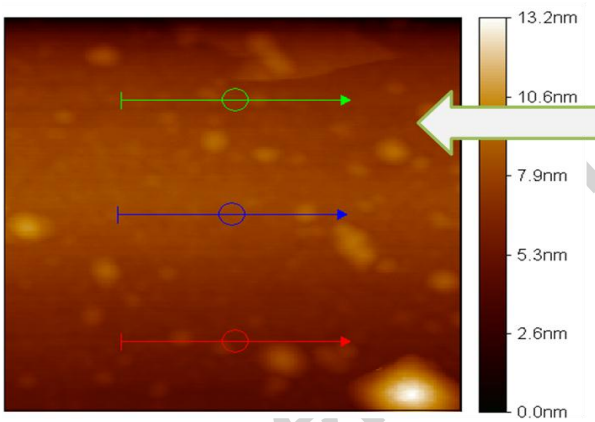

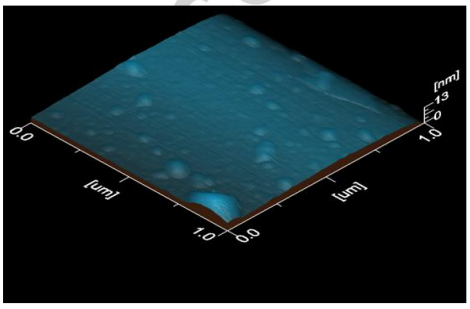

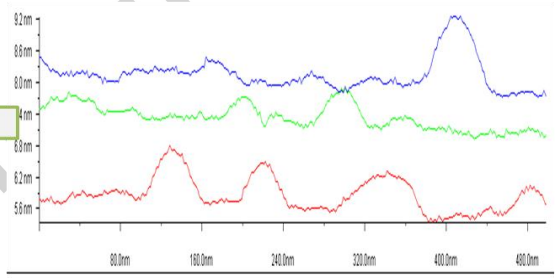

	1	2	3
Ra [nm]	0.250	0.188	0.209
Rzji [nm]	0.000	0.000	0.000
Rq [nm]	0.317	0.233	0.311
Rz [nm]	1.44	0.984	1.53
Length [nm]	0.498	0.498	0.498

Fig.6. AFM images of $Mg_{0.4}Cd_{0.1}Co_{0.5}Cr_{0.04}Tb_{0.02}Fe_{1.94}O_4$ spinel ferrite.

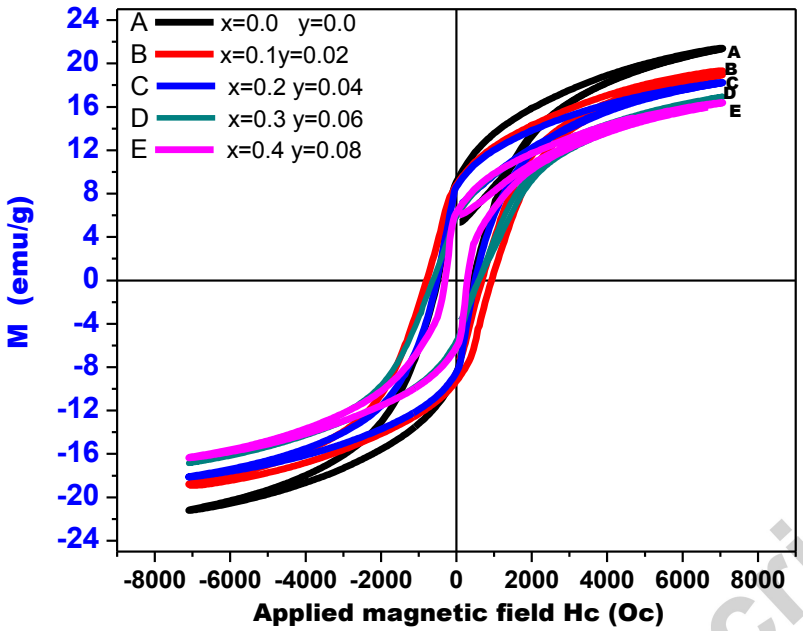

Fig.7. M-H loops for $Mg_{0.5-x}Cd_xCo_{0.5}Cr_{0.04}Tb_yFe_{1.96-y}O_4$ ferrite powders annealed at 850 ^oC.

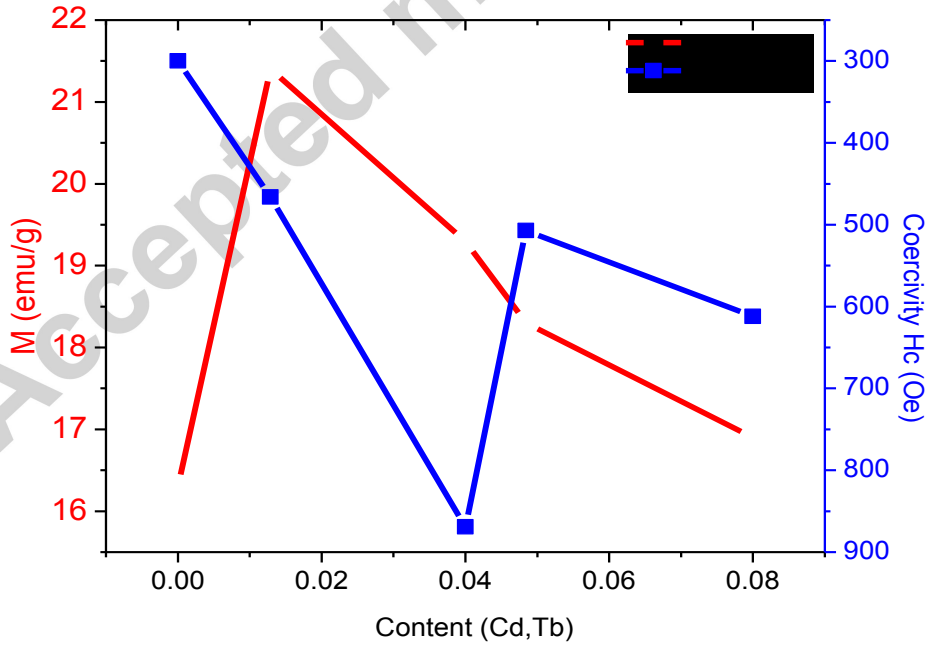

Fig.8. Variation of saturation magnetization and coercive field with co-substituted (Cd^{2+} Tb^{3+}) content for Mg-Co-Cr-Fe ferrites system

Research Highlights

- Effects of co-substitution (Cd^{2+}, Tb^{3+}) on structural and magnetic parameters are studied.
- XRD patterns revealed that first three samples are single phase while others are biphasic.
- The Ms was decreased from (21.4 - 16) emu/g with increasing co-substituted contents.
- The values of coercivity lie in range of (300 - 869) Oe for all samples of spinel ferrites.
- The results show that materials may have a potential for high density recording media.

List of Tables

Table 1

Average crystallite diameter (nm), cell volume (V), X-ray density and lattice strain for different co-substitution (Cd^{2+} Tb^{3+}) of the Mg-Co-Cr- Fe-O systems.

Parameters	x=0 y=0	x=0.1 y=0.02	x=0.2 y=0.04	x=0.3 y=0.06	x=0.4 y=0.08	x=0.5 y=0.10
Crystallite size $MCD_{<D>}$	36.6	44.2	65	69.4	40.3	68.3
Cell volume, (V)$Å^3$	598.48	590.46	599.21	600.784	602.77	586.07
X-ray density, g cm^{-3}	5.09	5.40	5.57	5.62	5.99	6.43
Lattice strain (ε_{rms})x10^{-3}	2.7	2.7	1.6	1.1	1.7	1.3

Table 2

Theoretical and observed lattice constant, Ionic radii of tetrahedral and octahedral sites (r_A, r_B), bond lengths (d_{AL} and d_{BL}) , tetrahedral and octahedral hopping lengths (L_A, L_B) , bond length cation-anion (Me-O) and cation-cation (Me-Me) at different co- substitution (Cd^{2+} Tb^{3+}) for Mg-Co-Cr- Fe-O ferrite system.

Table 3

The bond lengths between the cations (b, c, d, e and f) (Me–Me) and between the cation and anions (p, q, r and s) (Me–O) for different contents.

Samples Composition With Estimated Cations	(1) (a_{ob}) Å	(2) (a_{th}) Å	(3) r_A (Å)	(4) r_B (Å)	(5) d_{AL} (Å)	(6) d_{BL} (Å)	(7) L_A (Å)	(8) L_B (Å)
$Mg_{0.5}CO_{0.5}Cr_{0.04}Fe_{1.96}O_4$	8.427	8.326	0.609	0.679	1.959	2.029	3.649	2.979
$Mg_{0.4}Cd_{0.1}CO_{0.5}Cr_{0.04}Tb_{0.02}Fe_{1.94}O_4$	8.389	8.364	0.600	0.670	1.950	2.020	3.633	2.966
$Mg_{0.3}Cd_{0.2}CO_{0.5}Cr_{0.04}Tb_{0.04}Fe_{1.92}O_4$	8.431	8.402	0.610	0.680	1.960	2.030	3.651	2.981
$Mg_{0.2}Cd_{0.3}CO_{0.5}Cr_{0.04}Tb_{0.06}Fe_{1.90}O_4$	8.388	8.441	0.611	0.682	1.961	2.032	3.654	2.983
$Mg_{0.1}Cd_{0.4}CO_{0.5}Cr_{0.04}Tb_{0.08}Fe_{1.88}O_4$	8.457	8.479	0.616	0.686	1.966	2.036	3.662	2.990
$Cd_{0.5}CO_{0.5}Cr_{0.04}Tb_{0.1}Fe_{1.86}O_4$	8.369	8.517	0.595	0.665	1.945	2.015	3.624	2.959

Table 4 Saturation magnetization (emu/g), remanance (emu/g), Squareness ratio, Coercivity (Oe), magnetic moment, anisotropy constant (J/m^3) different co- substitution (Cd^{2+} Tb^{3+}) of the Mg-Co-Cr- Fe-O system.

	$(Me-O)$ Å				$(Me-Me)$ Å				
Sample	**p**	**q**	**r**	**s**	**b**	**c**	**d**	**e**	**f**
0.0, 0.0	0.951	3.825	7.325	4.316	2.979	3.493	3.648	5.473	5.160
0.1, 0.02	0.947	3.808	7.292	4.296	2.965	3.477	3.632	5.448	5.137
0.2, 0.04	0.951	3.827	7.328	4.318	2.980	3.495	3.650	5.476	5.162
0.3, 0.06	0.954	3.837	7.334	4.321	2.993	3.498	3.653	5.480	5.167
0.4, 0.08	0.954	3.839	7.351	4.331	2.990	3.506	3.661	5.492	5.178
0.5, 0.10	0.944	3.799	7.275	4.286	2.958	3.469	3.623	5.435	5.124

Parameters	**x=0 y=0**	**x=0.1 y=0.02**	**x=0.2 y=0.04**	**x=0.3 y=0.06**	**x=0.4 y=0.08**	**x=0.5 y=0.10**
Saturation Magnetization Ms (emu/g)	21.4	19.3	18.3	16.9	16.3	----
Remanance Mr (emu/g)	9.1	8.8	8.6	5.9	6.3	----
Squareness ratio (Mr/Ms)	0.42	0.46	0.47	0.35	0.38	----
Coercivity (Oe)	466	869	507	612	300	----
Magnetic Moment $n_B(\mu_B)$	0.88	0.83	0.82	0.79	0.79	----
Anisotropy Constant J/m^3	6.3	10.6	5.8	6.5	3	----